Chemosynthesis enhances carbon fixation in an active microbialite ecosystem

Francesco Ricci[1,2,3], Pok Man Leung[1,2,*], Tess Hutchinson[1,2], Thanh Nguyen-Dinh[1,2], Ashleigh v.S. Hood[3], Vinícius W. Salazar[4], Vera Eate[5], Wei Wen Wong[5], Perran L.M. Cook[5], Chris Greening[1,2] & Harry McClelland[3,6,*]

1. Department of Microbiology, Biomedicine Discovery Institute, Monash University, Melbourne, VIC, Australia
2. Securing Antarctica's Environmental Future, Monash University, Melbourne, VIC, Australia
3. School of Geography, Earth and Atmospheric Sciences, University of Melbourne, Parkville, VIC, Australia
4. Melbourne Bioinformatics, University of Melbourne, Parkville, VIC, Australia
5. Water Studies Centre, School of Chemistry, Monash University, Clayton, VIC, Australia
6. Department of Structural and Molecular Biology, University College London, London, WC1E6BT, UK

*Corresponding authors: francesco.ricci@monash.edu, bob.leung@monash.edu, and h.mcclelland@ucl.ac.uk

Abstract

Microbialites—carbonate structures formed under the influence of microbial action—are the earliest macroscopic evidence of life. For three billion years, the microbial mat communities responsible for these structures fundamentally shaped Earth's biogeochemical cycles. In photosynthetic microbial communities, light energy ultimately drives primary production and the ensuing cascade of daisy-chained metabolisms. However, reduced compounds such as atmospheric trace gases and those released as metabolic byproducts in deeper, anaerobic regions of the mat, could also fuel chemosynthetic processes. Here, we investigated the intricate metabolic synergies that sustain microbialite community nutrient webs. We recovered 331 genomes spanning 40 bacterial and archaeal phyla, revealing a staggering diversity fuelled by the biogeochemistry of these ecosystems. While phototrophy is an important metabolism encoded by 17% of the genomes, over half

encode enzymes to harness energy from reduced compounds and 12% co-encode carbon fixation pathways, using sulfide and hydrogen as major electron donors. Consistent with these genomic predictions, we experimentally demonstrated that microbialite communities oxidise ferrous iron, ammonia, sulfide and gas substrates aerobically and anaerobically. Furthermore, ^{14}C-fixation assays revealed that chemosynthesis contributes significantly to carbon fixation alongside photosynthesis. Chemosynthesis in microbialite communities represents a complex interplay of metabolic synergies and continuous nutrient cycling, which decouples community carbon fixation from the diurnal cycle. As a result, this process mitigates the loss of organic carbon from respiration, thus enhancing the net productivity of these highly efficient ecosystems.

Introduction

Complex microbial communities in aquatic environments can form carbonate structures named microbialites. With the earliest fossils dating to around three and a half billion years[1,2], these structures are representative of the most ancient and persistent microbial ecosystems in Earth's history. Over Earth's long history, dense, benthic microbial communities played a pivotal role in shaping the composition of Earth's atmosphere[3,4]. Notably, they contributed to the rise in atmospheric oxygen following the evolution of oxygenic photosynthesis[3,5], which amplified global biological productivity by 100-1000 fold[6]. Much of this new productivity first occured in microbial mats that provided favourable conditions for photosynthetic communities to thrive[7–9]. Additionally, mat communities mediated large fluxes of reduced gases such as carbon monoxide (CO), hydrogen (H_2), and methane (CH_4) into the atmosphere[6]. Today, living microbialites are generally confined to extreme environments such as hypersaline lakes[10–14], where grazing metazoans and plants are typically absent[3]. However, modern stratified microbial communities have a structure resembling those from the Cambrian[15] and Archaean[5], positioning these communities as natural laboratories for unravelling the functional processes underlying these ancient systems.

Microbialites are hotspots of microbial diversity[16–18], yet the key processes that have sustained the ecosystems associated with these structures remain enigmatic. Light is thought to have had a central role throughout their history, initially sustaining anoxygenic phototrophs and later cyanobacteria and algae, driving organic carbon production, carbonate precipitation, and elemental cycling[5,6,19,20]. The resultant photosynthetic end-products shape aerobic niches and fuel complex microbial networks[3], including by supporting the activity of aerobic heterotrophs[21–23]. Anaerobes dominate beneath the surface of microbial mats, including fermenters,

sulfate-reducing bacteria (SRB), and methanogens that catabolise organic matter and gases[6,24,25]. SRB use organic (e.g. acetate, sugars) and inorganic electron donors (e.g. H_2) while releasing H_2S. Chemolithoautotrophs can exploit inorganic compounds, encoding genes mediating the oxidation of H_2, CO, and various sulfur compounds[26–28], though their ecological and biogeochemical roles within these ecosystems remain poorly understood. While photosynthetic carbon fixation is central to biomass production in these ecosystems[3,29], this is not the sole process contributing to their primary production. Most notably, the abundant anoxic pockets within microbialites foster ecological niches well-suited for anaerobic autotrophs utilising the Wood–Ljungdahl pathway (WLP)[30–32]. Although gene- and genome-resolved studies have provided insights into the functional potential of microbialite communities, direct activity-based evidence of the complex metabolic interactions that sustain these ecosystems remains limited.

Here we aim to shed light on the primary production and elementary cycling processes sustaining the biodiversity of calcyfing microbial mats using living microbialites from West Basin Lake, Victoria, Australia. While it is recognised that microbialite communities have the potential for several photosynthetic and chemosynthetic carbon fixation pathways, we still lack a comprehensive understanding of their mediators, the role of various electron donors in driving these processes, and their relative contribution to primary production. The classic view positions photosynthesis as a leading process driving biological productivity[3,6,33,34]. However, microbialite communities produce substantial amounts of reduced compounds such as H_2, H_2S, CO and CH_4[6,25], which could fuel diverse chemosynthetic processes. Using living microbialite ecosystems, we integrate genome-resolved metagenomics with high-resolution metabarcoding, biogeochemistry, modelling and phylogenetic analysis to quantify the key metabolisms and their contributions in supporting the nutrient web in microbialite communities.

Results & Discussion

Taxonomically and metabolically diverse microbes control a complex nutrient web in living microbialites

We deeply sequenced nine metagenomes across three microbialite communities from West Basin Lake in Victoria, Australia. This effort resulted in the recovery of 331 medium- to high-quality metagenome-assembled genomes (MAGs) dereplicated

at the species level using a 95% ANI threshold. These MAGs depict a remarkable diversity spanning 40 bacterial and archaeal phyla, including the first genomes from a microbialite community for the phyla JAHJDO01 and UBP6 (Fig. 1). Many of these microbes represent elusive and rare lineages, such as Cloacimonadota, Krumholzibacteriota, Hydrogenedentota, Omnitrophota, and Sumerlaeota. Representatives of these phyla have been previously found in extreme environments including an Antarctic lake[35], deep-sea trenches[36] and geothermal springs[37]. The most abundant phyla were Proteobacteria and Bacteroidota, represented by 81 and 56 MAGs respectively (Fig. 1). Cyanobacteria are considered key members of these ecosystems, though we only retrieved one medium-quality MAG of *Halothece* (total rel. abundance 3.11%) and 18 MAGs capable of anoxygenic chlorophototrophy (Fig. 1). Millimeter-scale 16S rRNA gene community profiling detected 30 cyanobacterial sequences, which were present at considerably different relative abundance between the analysed samples (sample C: 11.2% ± 7.6; sample D: 0.27% ± 0.35) (Supp. Data 1). Archaea are also significant members, represented by 18 MAGs spanning Asgardarchaeota, Halobacteriota, Iainarchaeota, Nanoarchaeota, Thermoplasmatota and Thermoproteota (Fig. 1). Eukaryotes have been found in most modern microbial communities[38–40] and accordingly we identified several major members of diatoms and red and green algae (Supp. Data 1).

Screening of key metabolic pathways in the MAGs revealed extensive metabolic diversity within West Basin Lake microbialite communities (Fig. 1), potentially underpinning these diverse microbial assemblages. Many microbes appeared to be facultative anaerobes that can input electrons from organic carbon to aerobic and anaerobic respiratory chains with 63% of genomes encoding at least one terminal oxidase (Supp. Data 2). The widespread capacity to oxidise various inorganic compounds (53.2% of the genomes), including hydrogen, sulfide, and carbon monoxide, for supplemental energy likely allows more efficient use of organic carbon for anabolism than catabolism (Supp. Data 2). Furthermore, our data suggest that at West Basin Lake, most organic carbon is produced *in situ*. We identified multiple lines of evidence supporting this hypothesis. First, the lake is not connected to any inlet and lacks aquatic vegetation. Second, we measured moderate concentrations of organic carbon in the water, averaging 4.83 mg/L. Notably, organic carbon abundance increases on average from 3.09 mg/L in shallow to 5.60 mg/L in deeper layers within the microbialites (Supp. Data 3). Third, 13.6% of the generated MAGs encode genes for carbon fixation (Fig. 1). Specifically, 19 MAGs encoded the WLP, whereas 15 MAGs co-encoded the CBB cycle with several other energy harvesting genes (Fig. 1; Supp. Data 2). Interestingly, some MAGs possess the genetic machinery to utilise multiple energy sources. For instance, a *Thiohalophilus* MAG encodes the CBB cycle with uptake [NiFe]-hydrogenases, sulfide quinone oxidoreductase, thiosulfohydrolase, reverse dissimilatory sulfate reductase and iron oxidising cytochrome (Fig. 1). We also found six MAGs encoding the reductive tricarboxylic acid cycle (rTCA), three of which belonged to the enigmatic group 3 [NiFe]-hydrogenase-encoding Thermoplasmatota class E2 (Fig. 1). Lastly,

phototrophy based carbon-fixation via the CBB cycle was mediated by members of the Cyanobacteria, Proteobacteria and Gemmatimonadota (Supp. Data 2) as well as microalgae in the phyla Cercozoa, Chlorophyta, Gyrista and Rhodophyta (Supp. Data 1).

To gain a comprehensive, contextual understanding of the metabolic traits supporting energy conservation and primary production in microbialite communities, we conducted a comparative gene-centric analysis of West Basin Lake metagenomes alongside previously sequenced datasets, including thrombolite, oncolite, and stromatolite communities from five global sites (Fig. 1). The capacity for carbon fixation was consistently high across microbialites worldwide. In West Basin Lake, the CBB (*rbcL* av. 19.6%) and the WLP (*acsB* av. 9.92%) were predominant. In the global datasets, the CBB was also the major pathway (av. 32.5 ± 17.0%), while the WLP and 3-hydroxypropionate cycle showed occasional dominance in specific samples (Fig. 1). The potential to utilise inorganic substrates exhibited significant parallels across sites. Sulfide and H_2 appear to be dominant energy sources, reflected by the widespread oxidation capacity (*sqr*: West Basin Lake av. 60.9%, global 40.1 ± 20.9%; Group 1-3 NiFe hydrogenase: West Basin Lake av. 24.4%, global 22.2 ± 16.0%). The capacity for CO and arsenite oxidation–ancient metabolic traits–was also substantial across all microbial communities (*cooS & coxL*: West Basin Lake av. 17.7%, global 11.2 ± 11.7%; *aro*: West Basin Lake av. 11.5%, global 10.1 ± 7.3%). Conversely, photosynthesis genes showed some variation. West Basin Lake had moderate capacity for chlorophylls and bacteriochlorophylls mediated phototrophy (*psaA, psbA:* av. 21.9%) and microbial rhodopsins mediated phototrophy (*rho:* av. 30.5%), whereas the global datasets exhibited broader ranges (*psaA, psbA:* 12.6–141.3%; *rho:* 13.1–113.5%). This variability most likely underscores the influence of local environmental conditions on energy acquisition strategies. Overall, our findings demonstrate that the genetic potential for energy conservation and carbon fixation in West Basin Lake microbialites is broadly representative of other microbial communities forming microbialites that have been studied globally. The high metabolic flexibility observed in these ecosystems enables them to act as efficient engines of biological productivity, supporting diverse and dynamic microbial communities.

Tight microbial interactions support intricate biogeochemical cycles

Consistent with previous work[13,18,28,41,42], our findings reveal that microbialite communities have remarkable metabolic diversity, and we sought to resolve the

complex molecular interactions underpinning such diversity. Millimeter-scale community analysis revealed high microbial richness throughout the entire microbialite structure (Supp. Fig. 1). While some taxa such as fermenters in the order Clostridiales were confined to deeper anoxic niches (grey layer - Supp. Data 1), many other microbes were distributed across the whole microbialite structure (Supp. Data 1), most notably Cyanobacteriales and the sulfur-oxidiser Campylobacterales (Supp. Data 1). Similarly, members of the obligately anaerobic order Spirochaetales were ubiquitous (Supp. Data 1). These data suggest that the spatiotemporal physicochemical shifts such as the expansion of oxic pockets during the day foster tight metabolic interaction that allow diverse functional guilds to coexist and meet their physiological needs throughout the microbialite structure.

We developed a model to elucidate the array of molecular exchanges occurring within microbialite communities (Fig. 2). Molecular hydrogen (H_2) emerges as a central molecule. In these communities, H_2 is primarily produced through fermentation of photosynthetically- and chemosynthetically-derived organic carbon via diverse group 3 [NiFe]-hydrogenases and [FeFe]-hydrogenases, encoded by 90 and 55 MAGs respectively (Fig. 2). The genetic potential for other fermentation pathways in the community is high, with many MAGs encoding marker genes associated with acetate (*acdA, ack, pta*), formate (*fdhA, fdoG, pflD*), and lactate (*ldh*; Supp. Data 5) fermentation. Diazotrophic Cyanobacteria and members of six other phyla (16 MAGs) may also contribute to H_2 release as an obligate by-product of the nitrogenase reaction. Upon diffusion into aerobic niches, H_2 is readily utilised by the abundant community of gas oxidisers spanning 25 phyla (106 MAGs; Fig. 2), which may utilise the electrons derived through this process for carbon fixation (Supp. Data 2). Anaerobic processes likely recycle much of the H_2, including through coupling to denitrification (109 MAGs) and dissimilatory nitrate reduction to ammonium (55 MAGs; Fig. 2). Hydrogenotrophic acetogens were found across each microbialite sample, albeit at low relative abundance (av. 1.2% of mapped reads). H_2 also fuels methanogenesis and sulfate reduction to varying degrees, leading to the production of methane and sulfide (Fig. 2). Aerobic and anaerobic CO oxidation are important processes within microbialite communities (34 MAGs; Fig. 2), capable of supporting energy conservation and carbon fixation in eight phyla (Supp. Data 2). A total of 78 MAGs, representing chemolithotrophic and photolithotrophic microorganisms across nine phyla, possess the potential to oxidize sulfide under both aerobic and anaerobic conditions (Fig. 2; Supp. Data 2). This capability likely provides a substantial ecological advantage, facilitating their persistence in environments characterised by dynamic redox fluctuations and intense resource competition.

Microbialite communities mediate broad aerobic and anaerobic elemental cycling

To validate our biogeochemical predictions, we performed *ex situ* microcosm experiments. The potential for oxygenic photosynthesis was assessed using chemical imaging that simultaneously visualises and quantifies O_2 concentrations in natural samples[43,44]. Algal and cyanobacterial populations, abundant in the microbialite communities, exhibited high activity, producing substantial O_2 when exposed to light intensities of ~450 µmol m^{-2} s^{-1}, mimicking their natural habitat (Fig. 3; Supp. Fig. 2). The well-illuminated microbialite surfaces demonstrated the highest gross O_2 production, though this varied markedly both within individual samples (e.g., Sample 2 ranged from 29.31 to 182.26 µmol O_2 L^{-1} min^{-1}) and among samples (Fig. 3; Supp. Fig. 2). Upon transition to darkness, O_2 was rapidly depleted, primarily through aerobic respiration and diffusion into the overlying water column (Fig. 3). The rapid O_2 consumption likely contributes to niches for the widespread facultative and obligate anaerobes at the millimetre-scale (Supp. Fig. 2). The O_2 generated via oxygenic photosynthesis also serves as an electron acceptor for several metabolic pathways, including organotrophy, hydrogenotrophy, carboxydotrophy, and nitrification. Correspondingly, all samples demonstrated oxidation of H_2, CO, and NH_4^-, albeit at varying rates (Fig. 3).

We observed consumption of H_2, CO, Fe^{2-}, and S^{2-} in nearly all anaerobic microcosms (Fig. 3), confirming the high metabolic flexibility of the anaerobic communities. This metabolic versatility aligns with genomic predictions made by previous studies in the literature[13,26,41] and reflects the capacity of microbialite communities to exploit alternative electron donors to sustain their nutrient web (Supp. Fig. 1). Such flexibility enables them to optimise energy generation across the dynamic physicochemical gradients of the microbialite environment. Consistent with these findings, physicochemical analyses revealed the presence of diverse electron acceptors in the microbialite samples. Specifically, SO_4^{2-} was present in high concentrations (av. 67.85 mg/L), whereas NO_3^- at moderate concentrations (av. 2 mg/L; Supp. Data 3).

Our genomic predictions further indicate that microbialites host microbial populations with high capacity for reductive metabolisms (Fig. 1). Microcosm experiments under prolonged anoxia confirmed the production of large amounts of reduced inorganic compounds (Fig. 3). Despite methanogens being low in abundance (av. *mcrA* 0.12% of the community), their elevated metabolic rates enable them to contribute notably to CH_4 production (av. 28.7 ppm/h; Fig. 3), a characteristic previously documented in other environments[45]. Similarly, sulfate reducers were scarce (av. *asrA, dsrA:* 2.44%) but released abundant S^{2-} (av. 7.4 µM/h; Fig. 3). On the other hand, fermenters (av. FeFe-hydrogenase: 34.37%; group 3 NiFe hydrogenase: 48.77%) and nitrogen fixer (av. *nifH:* 27.49%) abundance was mirrored in the high H_2

production (22.7 ppm/h; Fig. 3). These reduced compounds, diffusing through the microbialite structure, fuel a diverse array of aerobic and anaerobic metabolic pathways, thereby supporting microbial energy conservation and carbon fixation within these dynamic ecosystems.

Chemosynthesis and photosynthesis contribute significantly to microbialites' carbon fixation

While there's long-standing evidence for photosynthesis in microbial mats[19,46,47], recent genomic studies suggest chemosynthetic pathways also facilitate primary production[25–27,48], though current evidence is fragmentary. To gain a comprehensive understanding of the diversity of microbialite autotrophic populations, we performed phylogenetic analyses of carbon fixation protein sequences. These phylogenetic inferences were further supported by activity measurements using ^{14}C incorporation assays, conducted with a range of supplemental electron donors (Fig. 4). We analysed the phylogenies of protein sequences encoding the acetyl-CoA synthase (AcsB), ribulose 1,5-bisphosphate (RbcL) and ATP-citrate lyase (AclB) (Fig. 4a-c). This analysis revealed an extraordinary diversity of sequences affiliated with at least 16 phyla across the CBB, WLP and rTCA (Fig. 4a-c). These sequences encompassed multiple novel autotrophic clades including two Nanoarchaeota MAGs encoding the CBB, one JAHJDO01 MAG encoding the WLP, and one Polyangia MAG encoding the rTCA (Fig. 4a-c).

Across the 140 RuBisCO (RbcL) sequences, we recovered four subtypes (Fig. 4a). Notably, RuBisCO subtypes IA-D exhibit intermediate to high specificity for CO_2 and are generally found across both aerobic and anaerobic habitats, whereas RuBisCO subtype II has lower CO_2 specificity and is more commonly associated with anaerobic or microaerophilic environments[49]. Consistent with the prevalent anaerobic niches of most microbialites, we recovered 184 acetyl-CoA synthase (AcsB) protein sequences for the WLP (Fig. 4b). However, a large proportion of these sequences most likely were not encoded by autotrophs but rather by members of the phyla Actinomycetota, Desulfobacterota and Chloroflexota that generally utilise the reverse WLP for acetate oxidation coupled with dissimilatory sulfate reduction. Conversely, sequences associated with the Firmicutes, Planctomycetota and Spirochaetota likely represent carbon-fixing acetogens, consistent with prior studies characterizing these phyla[50,51].

To validate the potential for carbon fixation highlighted through genomic and phylogenetic analysis, we quantified relative chemosynthetic and photosynthetic

carbon fixation rates using radiolabeled carbon dioxide ($^{14}CO_2$). To capture both aerobic and anaerobic carbon fixation processes, we conducted five-day experiments, during which the microcosms transitioned to anaerobic conditions after approximately 24 hours. This transition was inferred based on O_2 measurements taken simultaneously on other microcosms. $^{14}CO_2$ incorporation was detected in all microcosms, except for H_2-stimulated chemosynthesis in microbialite C (Fig. 4d, Supp. Fig. 3), which most likely resulted from an experimental issue. As anticipated, microcosms exposed to light supported higher $^{14}CO_2$ incorporation through photosynthesis (av. 0.0122 nmol day^{-1} g wet^{-1}) compared to those incubated in the dark (av. 0.00279 nmol day^{-1} g wet^{-1}; Fig. 4d). Dark incubations likely captured the combined activity of anaplerotic processes and baseline chemosynthetic carbon fixation. The addition of electron donors significantly boosted chemosynthetic carbon fixation rates (Fig. 4d). Consistent with the high abundance of genes and MAGs encoding *sqr* and *rdsrA* genes (Fig. 1), S^{2-}-supplemented microcosms exhibited the highest chemosynthetic $^{14}CO_2$ incorporation rates (av. 0.0084 nmol day^{-1} g wet^{-1}). Similarly, NH_4^+ and H_2 supplementation enhanced chemosynthetic carbon fixation (av. 0.00741 and 0.0062 nmol day^{-1} g wet^{-1}, respectively; Fig. 4d). Contrary to the prevailing view that microbial productivity is predominantly driven by photoautotrophs, our findings reveal that inorganic chemical sources and gas substrates are also critical for the primary productivity of these ecosystems, highlighting the significant role of chemosynthesis in supporting stratified microbial communities.

Conclusions

Through an integrative approach, our study sheds light on the intricate molecular exchanges that underpin the carbon acquisition, energy conservation, and broader nutrient cycling within a model microbialite community, offering a detailed view into how taxonomic and metabolic diversity intersect in such ecosystems. Microbialite communities in the hypersaline West Basin Lake exhibit a metabolic diversity comparable to that observed in other microbialite ecosystems worldwide (Fig. 1). This diversity likely arises from the presence of organisms with complementary traits, driven by resource facilitation among community members[52,53]. In microbialite communities, metabolic synergies occur between organisms inhabiting contrasting physicochemical niches[26,54], which vary on adiel cycle The resultant mosaic of ecological niches align with the physiological requirements of diverse microbial taxa. Consistent with these observations, our analysis simultaneously reveals millimetre-scale overlap of functional guilds throughout the microbialite structure (Supp. Fig. 2) and cycling of key metabolites such as iron, nitrogen and sulfur compounds across

their major redox states through intricate molecular handoffs (Supp. Data 2). These processes promote minimal energy loss and enhance ecosystem productivity[55]. In a broader context, the exceptional efficiency of elemental cycling and carbon use efficiency within microbialite communities, combined with the duality of light- and chemically-driven metabolic pathways, suggests that these ecosystems have likely served as hotspots of metabolic innovation throughout Earth's history.

Methods

Characterization of microbial mat organosedimentary structures

The eastern shoreline of West Basin Lake hosts abundant microbialites and living microbial matgrounds[56]. Well-developed microbialite buildups and hardgrounds are exposed on subaerially-exposed benches up to several metres above the current lake level. Previous studies have documented extensive sub-aqueous, well-lithified living microbialites with considerable relief above the lake floor, especially in the adjacent East Basin Lake[56]. The living microbialites documented in this study occur in shallow water of around 0.5 m depth, and are best-developed in benches approximately 1-2 m from the current shoreline in West Basin Lake (Supp. Fig. 4). These living microbial matgrounds appear dark orange-red and have an irregular, undulating surface with a broad-scale relief of several centimetres. In cross section, the mats have a dark orange-red film over a hard to friable, mineralised, cream-white uppermost layer of up to several millimetres in thickness (Supp. Fig. 1). This mineralised layer has an irregular, pustular appearance and is composed of carbonate, likely hydromagnesite[56]. Underneath this, the mat consists of weakly lithified to unlithified mud with several thin colour zones over a several millimetres depth (dark green, purple and grey), followed by up to several centimetres of light green mat (Supp. Fig. 1; Supp. Fig. 4). The sediment texture is commonly clotted and unlaminated. The substrate for the mat is dark, organic-rich mud which may have weak layering preserved through the presence of occasional coarse sediment laminae. Here we use the term ‘microbialite’ to define these microbial matgrounds, as they do form mineralised structures with cm-scale relief above the lake floor. While these modern and recent microbialites are not as extensively developed as the sub-aerially exposed microbialites, they do appear to form significant accretionary structures over time (for example encrusting anthropogenic debris).

Sample collection, processing and physicochemical parameters

Forming microbialites were collected from West Basin Lake (38° 19' 24.6468" S, 143° 26' 51.8928" E), a hypersaline (salinity 6.5-9.5%) inland crater lake located in Victoria, Australia. Microbialites samples were collected during three field trips in November 2022, March 2024 and May 2024 using pre-sterilized spades and

transferred into pre-sterilized 5-gallon buckets containing lake water. At first collection in November 2022, the water temperature was 18.9 °C, dissolved oxygen 90%, pH 8.47 and oxidative reduction potential 2.72 mV. Irradiance at noon was measured using a Walz Universal Light Meter (ULM-500) equipped with a Mini Quantum Sensor (LS-C) at 30 cm and 50 cm below the water surface was ~650 µmol photons m^{-2} s^{-1} and ~450 µmol photons m^{-2} s^{-1}, respectively. Physicochemical parameters for lakewater and microbialite depth-profile subsamples were measured at the TrACEES Platform, University of Melbourne. The selected physicochemical parameters include total organic carbon, total carbon, inorganic carbon, total nitrogen, sodium, magnesium, potassium, calcium, sulfate and chlorum. Nitrate was measured at Water Studies, Monash University.

16S rRNA gene sequencing and community analysis

Total DNA was extracted from the layers of two different microbialite samples (three technical triplicate per layer) using the DNeasy PowerSoil Kit (Qiagen, Hilden, Germany) on 0.5g of material. Two sample-free negative control were also included. Extracted DNA samples were sent to AGRF (Melbourne, Victoria) for library preparation, PCR-amplification and sequencing of the 16S rRNA gene V1-V3 regions on an Illumina MiSeq platform, 2x300bp paired-end reads. Sequences were processed using the QIIME2 pipeline v 2022.2[57]. Primer sequences were trimmed using Cutadapt[58], while DADA2 was employed for merging forward and reverse reads, quality filtering, dereplication, and chimera removal[59]. Taxonomic classification was performed with QIIME2's feature-classifier plugin. The SILVA v132 QIIME release was used for 16S rRNA gene taxonomy[60].

Community DNA extraction and sequencing

Each microbialite sample was homogenised into a slurry. Total DNA was extracted from three different microbialite slurry samples (technical triplicate per sample for a total of nine samples) using the DNeasy PowerMax Soil Kit (Qiagen, Hilden, Germany) on 10 g of materials as per the manufacturer’s protocol. A sample-free negative control was also included. Extracted DNA samples were sent to AGRF (Melbourne, Victoria) for library preparation and sequencing on two lanes using an Illumina NovaSeq SP Flow-cell, 2 x 150 bp for 500 cycles.

Reads quality control, assembly and binning

Across the three technical replicates of each microbialite sample, we obtained an average of over 16 million read pairs for sample 1, over 56 million read pairs for sample 2, and over 40 million read pairs for sample 3. Reads quality control, assembly and binning were implemented within the Metaphor pipeline[61]. Specifically,

raw reads derived from the nine metagenome libraries were quality-controlled by trimming primers and adapters, followed by artefacts and low-quality read filtering using fastp[62] with parameters *length_required 50*, *cut_mean_quality 30*, and *extra: --detect_adapter_for_pe*. The nine quality-controlled metagenomes were coassembled using MEGAHIT v1.2.9[63] with default parameters. Contigs shorter than 1,000 bp were removed. Assembled contigs were binned using Vamb v4.1.3[64], MetaBAT v2.12.1[65] and CONCOCT v1.1.0[66]. The three bin sets were then refined using DAS Tool v1.1.6[67] and de-replicated using dRep v3.4.2[68] with 95% ANI integrated with CheckM2[69]. Bins completeness and contamination were estimated using CheckM2[69]. After dereplication, we recovered 331 between medium (completeness >50%, contamination <10%) and high-quality (completeness >90%, contamination <5%) metagenome-assembled genomes (MAGs), according to the MIMAG standard[70]. MAG taxonomy was assigned according to Genome Taxonomy Database Release R214[71] using GTDB-Tk v2.3.2[72]. CoverM v0.6.1 was used to calculate the relative abundance of bins based on the metagenomic reads (https://github.com/wwood/CoverM).

Functional annotation of binned contigs and unbinned contigs

The sequences of 51 marker genes representing energy conservation, carbon fixation, trace gas metabolism, sulfur cycle, nitrogen cycle, arsenic cycle, iron cycle, formate oxidation, phototrophy, and aerobic respiration were retrieved from the 331 MAGs and unbinned contigs. Open reading frames (ORFs) were predicted using Prodigal v2.6.3[73], then annotated using DIAMOND blastp[74] homology-based searches against a custom database[75] of 51 metabolic marker gene sets described below. DIAMOND mapping was performed with a query coverage threshold of 80% for all databases, and a percentage identity threshold of 80% (for *psaA*) 75% (for *mcr, hbsT*), 70% (for *isoA, psbA, ygfK, aro, atpA*), 60% (*amoA, pmoA, mmoA, coxL, [FeFe], nxrA, rbc, nuoFL*) or 50% (all other databases). MAGs were also annotated using DRAM[76].

Metabolic annotation of metagenomic short reads

Paired-end reads from the nine samples were stripped of adapter and barcode sequences, then contaminating PhiX and low-quality sequences were removed (minimum quality score 20) using the BBDuk function of BBTools v.36.92 (https://sourceforge.net/projects/bbmap/). Resultant quality-filtered forward reads with lengths of at least 100 bp were searched for the presence of the 51 marker genes described above using the DIAMOND blastx algorithm[77]. Specifically, reads were compared against the custom-made reference databases[75] of 51 metabolic marker genes for energy conservation, carbon fixation, phototrophy, and hydrogen,

carbon monoxide, methane, sulfur, nitrogen, and iron cycling. A query coverage of 80% and an identity threshold of 80% (for *psaA*), 75% (for *hbsT*), 70% (for *atpA, psbA, isoA, ygfK, aro*), 60% (for *amoA, mmoA, coxL, FeFe, nxrA, rbcL, nuoF*) and 50% (for all others) was used. The proportion of community members encoding each gene was calculated by normalizing the gene's read count (measured in reads per kilobase million [RPKM]) against the average RPKM of 14 universal single-copy ribosomal marker genes.

Phylogenetic analysis

Maximum-likelihood phylogenetic trees for archaeal and bacterial MAGs were built using GTDBtk[72] commands *identify* and *align* on high quality MAGs (completion >90% and contamination <5%). The archaral and bacterial trees were built using IQ-TREE v2.2.2.6[78,79] with 1,000 ultrafast bootstrap[80] using the LG+C10+F+G and WAG+G20 models, respectively. MUSCLE[81] was used to align 36 AclB, 184 AcsB and 140 RbcL proteins retrieved between the MAGs and unbinned contigs. Aclb, AcsB and RbcL maximum-likelihood phylogenetic trees were built using IQ-TREE v2.2.2.6[78,79] with 1,000 ultrafast bootstrap[80] and models LG+F+I+R6 for the AcsB tree, LG+I+G4 for the AclB tree and LG+R5 for the RbcL tree. All trees were plotted using iTOL v6[82].

Chemical imaging

The O_2 sensitive optode preparation included mixing 100 mg of polystyrene, 1.5 mg of indicator (PT (II) meso-tetra(pentafluorophenyl)porphine), 1.5mg of reference (Macrolex yellow®) and dissolved in 1 g of solvent (Tetrahydrofuran) to form a cocktail. The O_2 cocktails were knife-coated on dust-free polyester foils (goodfellow.com) and the final thickness of the coating was <2 µm. Once dry, the O_2 sensitive optode was coated with an antirefractory layer. The antirefractory cocktail preparation included mixing 100 mg hydrogel D4, 100mg carbon black and 1 g of 100% ethanol. The antirefractory cocktail were knife-coated on top of the O_2 sensitive optode and the final thickness of the coating was <3 µm.

The experimental setup included a modified digital single-lens reflex camera (Canon EOS 1000D) with its near-infrared (NIR) blocking filter removed and equipped with a Sigma 50 mm F2.8 EX DG Macro lens. An emission filter (Schott 530 nm, Uqgoptics.com) was fitted to the lens to detect oxygen fluorescence. Following the protocol described by Larsen et al. (RED), O_2 sensitive optode were excited by four high-power blue LEDs (l-peak = 445 nm, LXHL-LR3C, Luxeon, F = 340 mW at IF = 700 mA) combined with a 470 nm short-pass filter (blue dichroic color filter, Uqgoptics.com). Microbialite sample cross-sections were illuminated using a Schott

Leica KL 2500 LCD Cold Light Source. All components were synchronized via a trigger box (https://imaging.fish-n-chips.de) and controlled using the custom software Look@RGB. Each planar optode was calibrated individually in an aquarium maintained at a constant seawater temperature of 20 ± 1°C in a darkened room. The calibration range for the O_2 sensitive optode was 0 – 360 µmol L^{-1}.

All experiments were conducted in a dark room at a constant 20 ± 1 °C to resemble the lake temperature at the time of sampling. Three microbialite samples were cut using a diamond saw exposing their cross-sections. Each of these samples was placed in a 4 L glass aquarium pressing on the O_2 sensitive optode, which was attached to the aquarium side. Following overnight acclimation in the aquaria, microbialite sample cross-sections were illuminated from above with approximately 450 µmol m^{-2} s^{-1} of light. Irradiance levels in the experimental setup for defined lamp settings were measured using a Walz Universal Light Meter (ULM-500) equipped with a Mini Quantum Sensor (LS-C). Image sequences capturing O_2 dynamics across the microbialite cross-sections were taken every 5 minutes. Lake water in the aquarium was aerated with an aeration stone connected to an air pump.

Downstream data analysis was conducted using ImageJ v1.53K. Each image was separated into Red, Green, Green2, and Blue RAW TIFF channels. The ImageJ plugin Ratio Plus was used to calculate the ratio of the Red to Green channels (R/G). The resulting ratio images were color-coded using the 'Fire' lookup table to visualise O_2 dynamics. Calibration was performed using the Curve Fitting function, applying an exponential fit with offset for O_2, based on planar optode calibration values. Brightness and contrast settings were adjusted to display minimum and maximum values of 0 – 360 µmol L^{-1} for O_2 images. To minimize influence of water infiltrating in between the O_2 optode and microbialite cross-section and to quantify microbial O_2 production, the first image of each experiment was subtracted from subsequent images using the Image Calculator function. To identify the photosynthetic regions on the microbialite sample cross-sections, we overlaid images with the highest O_2 production onto microbialite cross-section images. The portions of each microbialite sample that showed O_2 production were identified as regions on interes (ROI). Subsequently values were extracted from the ROI. Control sample in Fig. 3 was an image sequence of ROI measuring a deeper, anaerobic microbialite cross-section portion simultaneously to O_2 measurements. Proxies for the net photosynthesis (PN) and apparent dark respiration (RD) were calculated by subtracting images taken with a 5 min interval when O_2 production and respiration were the highest, respectively. Gross photosynthesis was estimated as PG = PN+|RD|.

Ex-situ biogeochemical measurements

We conducted microcosm experiments to evaluate the aerobic and anaerobic metabolism of microbialite communities. Each experiment was performed in triplicate, with three independent microbialite samples per replicate. Heat-killed samples were prepared using gamma radiation followed by one autoclave cycle at 121 °C for 30 minutes and served as controls. These controls confirmed that the observed element dynamics were attributable to biotic processes.

Aerobic and anaerobic microcosms, including trace gas and S^{2-} and Fe^{2+} additions, were set up in 120 mL serum vials containing 50 mL of 0.22 µm-filtered lake water and approximately 10 g of microbialite to create slurries. The vials were sealed with butyl rubber septa. For aerobic microcosms, the headspace was left with ambient air, while anaerobic microcosms were flushed with helium for 10 minutes to remove O_2 and then supplemented with 1.5 mM NO_3^- as an electron acceptor (except for S^{2-} consumption). The weights of microbialite used in each microcosm were recorded and used to normalise downstream calculations.

Trace gas microcosms were supplemented with 10 ppm H_2, CH_4, and CO in the headspace. Sampling of the headspace began immediately after the addition of electron donors and acceptors, with 2 mL of gas extracted at variable time intervals as shown in Fig. 3. In anaerobic vials, the sampled gas volume was replaced with He. Gas concentrations were analysed by gas chromatography using a pulsed discharge helium ionization detector (model TGA-6791-W-4U-2, Valco Instruments Company Inc.), with calibration based on certified standard mixtures of H_2, CH_4, and CO (0, 10, 100 ppm in N_2, BOC Australia).

In anaerobic S^{2-} and Fe^{2+} microcosms, either 100 µM Na□S·9H□O (only for consumption) or 6 mM FeCl□ was added to helium-purged slurries. At each timepoint, 3 mL of water was sampled and filtered through 0.45 µm pore-size filters. For S^{2-} analysis, 2 mL of the filtered sample was preserved with ZnAc, while for Fe^{2+} analysis, 1 mL was preserved with ferrozine. Both S^{2-} and Fe^{2+} concentrations were measured using a GBC UV-Visible 918 spectrophotometer, following methods described previously[83].

Microcosms for nitrification were prepared in uncapped 250 mL Schott bottles containing 100 mL of 0.22 µm-filtered lake water, 100 µM NH_4^+, and approximately 10 g of microbialite sample. At each sampling timepoint, 10 mL of water was filtered through 0.45 µm pore-size filters and stored frozen until further analysis. The filtered samples were analysed for NOx (NO_2^- + NO_3^-) concentrations using a Lachat QuikChem 8000 Flow Injection Analyzer (FIA) in accordance with APHA methods[84]. For oxygen measurements, microcosms were prepared in 120 mL vials containing 100 mL of 0.22 µm-filtered lake water and approximately 10 g of microbialite slurry. Dissolved O_2 concentrations were monitored using a FireSting oxygen probe (PyroScience) until the microcosms approached anoxic conditions.

^{14}C incorporation analysis

0.25 g of homogenised microbialite sample with 1 mL of filtered lake water (0.22 µm) were prepared in 7 mL scintillation vials with ambient air headspaces. Radiolabeled sodium bicarbonate solution ($NaH_{14}CO_3$, Perkin Elmer, 53.1 mCi $nmol^{-1}$) was added to a concentration ~0.1 µM. Triplicates of each sample were prepared and subjected to five different conditions, namely light (40 µmol m^{-2} s^{-1}), dark, dark + H_2 (100 ppm), dark + S^{2-} (800 µM) and dark + NH_4^+ (1 mM) and incubated for 5 days. These experiments aimed at capturing both aerobic and anaerobic carbon incorporation metabolisms and according to parallel O_2 measurements, microcosms likely transitioned to anaerobic after approximately 24 h. After the incubation period, concentrated HCl was added dropwise to each vial and left for 24h with intermittent shaking to ensure excess unbound dissolved inorganic carbon (DIC) was acidified and released as $^{14}CO_2$. HCl was added equally to all vials until bubble production ceased and then they were placed at 60 °C under a heat lamp to dry. When dry, 7 mL of scintillation liquid (EcoLume™, MP Biomedical) was added and ^{14}C measured on an automated liquid scintillation counter (Tri-Carb 2810 TR, Perkin Elmer). Photosynthetic ^{14}C incorporation values were adjusted to account for the photosynthetic ROI areas present on the 0.25g portion of microbialite used in the light treatment. Assuming that the photosynthetic ROI areas identified through chemical imaging represent the microbialite sample regions performing oxygenic photosynthesis, we normalised by applying the ratio of photosynthetic ROI area of microbialite sample 3 which had the largest photosynthetic surface area (photosynthetic ROI sample 1: 3.11%, sample 2: 2.73%, and sample 3: 6.35%) to total microbialite area. We developed a hierarchical Bayesian model to analyze ^{14}C incorporation rates under different conditions. The model is implemented in Stan and R (see SI for code). The model consists of N total observations, with I samples, J conditions, and K replicates for each sample condition combination. As the Dark+H_2 condition experiment failed for microbialite C, we ran two models: one excluding microbialite C and included all conditions (where I=2, J=5, K=3 and N=30), and one excluding the Dark+H_2 condition and included all samples (where I=3, J=4, K=3 and N=36), so that in each case the model can be fitted to a complete dataset. The likelihood function is given by:

$$y_{ijk} \sim N(\alpha_i + \beta_j, \sigma^2),$$

where α_i describes the sample specific effect for the ith sample, β_j describes the condition specific effect for the jth sample, and σ^2 is the unexplained variance in the data. The Dark condition (j=1) was prescribed to be the control by setting $\beta_1 = 0$. Weakly informative priors were used. Priors for α_i ($i \in \{1:I\}$) and β_j ($j \in \{2:J\}$) were specified as normal distributions with variances an order of magnitude larger than the variance of the total dataset. The prior for σ was a Cauchy distribution. Posterior probability distributions for values of β are presented in figure 4D, with

Credible intervals defined between the 2.5th and 97.5th, and the 25th and 75th percentiles.

Statistics and visualization

Downstream statistical analyses were performed in RStudio (version 1.2.5033) using several R packages, including decontam[85], ggplot2[86], phyloseq[87], and vegan[88]. Illustrator v24.0.2 was utilised for figure editing.

Data availability

All data supporting the findings of the present study are available. We deposited all the project's sequences at the Sequence Read Archive. Metagenomic sequences have accession number PRJNA1194634, 16S rRNA gene sequences have accession number PRJNA1194668, and MAGs have been submitted and awaiting release.

Conflict of interest

The authors declare no conflict of interest.

Acknowledgments

We acknowledge Judy and Leon for kindly allowing us to conduct our study on their property at West Basin Lake. F.R. was supported by the Early Career Postdoctoral Fellowship (ECPF24-4273843556) awarded by the Faculty of Medicine, Nursing and Health Science at Monash University, and internal funding awarded to H.M. from the University of Melbourne. P.M.L. was supported by an ARC DECRA Fellowship (DE250101210). C.G. was supported by an NHMRC EL2 Fellowship (APP1178715). A.H. was supported by an ARC DECRA Fellowship (DE190100988). This study used the MASSIVE M3 supercomputing infrastructure.

Author contribution

F.R., C.G., P.M.L., and H.M. conceptualised the study. Experimental planning and design were conducted by F.R., C.G., T.H., V.E., W.W.W., and P.C. Fieldwork was conducted by F.R., H.M. and A.H. A.H. provided microbialite description. Data analysis was led by F.R. Gas chromatography measurements were carried out by F.R., T.H., and T.N., while V.E. and W.W.W. oversaw nitrification measurements. Chemical imaging, oxygen, sulfide and ferrous oxide measurements were performed by F.R. Carbon fixation incubations were performed by T.H. Metagenome analysis, MAG construction, and annotation were completed by F.R., with extensive bioinformatics support provided by V.W.S. Resources, supervision, and funding were contributed by C.G., P.C., and H.M. The manuscript was written by F.R., with input from all authors.

References

1. Walter, M. R., Buick, R. & Dunlop, J. S. R. Stromatolites 3,400–3,500 Myr old from the North pole area, Western Australia. *Nature* **284**, 443–445 (1980).
2. Van Kranendonk, M. J., Philippot, P., Lepot, K., Bodorkos, S. & Pirajno, F. Geological setting of Earth's oldest fossils in the ca. 3.5 Ga Dresser formation, Pilbara Craton, Western Australia. *Precambrian Research* **167**, 93–124 (2008).
3. Dick, G. J., Grim, S. L. & Klatt, J. M. Controls on O_2 Production in Cyanobacterial Mats and Implications for Earth's Oxygenation. *Annu. Rev. Earth Planet. Sci.* **46**, 123–147 (2018).
4. Cavalier-Smith, T. Cell evolution and Earth history: stasis and revolution. *Phil. Trans. R. Soc. B* **361**, 969–1006 (2006).
5. Nisbet, E. G. & Fowler, C. M. R. Archaean metabolic evolution of microbial mats. *Proc. R. Soc. Lond. B* **266**, 2375–2382 (1999).
6. Hoehler, T. M., Bebout, B. M. & Des Marais, D. J. The role of microbial mats in the production of reduced gases on the early Earth. *Nature* **412**, 324–327 (2001).
7. Des Marais, D. J. Earth's early biosphere. *Gravitational and space biology bulletin: publication of the American Society for Gravitational and Space Biology* **11**, 23–30 (1998).
8. Hawes, I., Sumner, D. Y., Andersen, D. T., Jungblut, A. D. & Mackey, T. J. Timescales of growth response of microbial mats to environmental change in an ice-

covered Antarctic lake. *Biology* **2**, 151–176 (2013).

9. Nold, S. C. *et al.* Underwater sinkhole sediments sequester Lake Huron's carbon. *Biogeochemistry* **115**, 235–250 (2013).

10. Boidi, F. J., Mlewski, E. C., Gomez, F. J. & Gérard, E. Characterization of Microbialites and Microbial Mats of the Laguna Negra Hypersaline Lake (Puna of Catamarca, Argentina). in *Microbial Ecosystems in Central Andes Extreme Environments* (ed. Farías, M. E.) 183–203 (Springer International Publishing, Cham, 2020). doi:10.1007/978-3-030-36192-1_13.

11. Paul, V. G., Wronkiewicz, D. J., Mormile, M. R. & Foster, J. S. Mineralogy and Microbial Diversity of the Microbialites in the Hypersaline Storr's Lake, the Bahamas. *Astrobiology* **16**, 282–300 (2016).

12. Bischoff, K. *et al.* Spherulitic microbialites from modern hypersaline lakes, Rottnest Island, Western Australia. *Geobiology* **18**, 725–741 (2020).

13. Osman, J. R. *et al.* Key energy metabolisms in modern living microbialites from hypersaline Andean lagoons of the Salar de Atacama, Chile. *Science of The Total Environment* **937**, 173469 (2024).

14. Pace, A. *et al.* Microbial and diagenetic steps leading to the mineralisation of Great Salt Lake microbialites. *Scientific Reports* **6**, 31495 (2016).

15. Laval, B. *et al.* Modern freshwater microbialite analogues for ancient dendritic reef structures. *Nature* **407**, 626–629 (2000).

16. Valdespino-Castillo, P. M. *et al.* Exploring biogeochemistry and microbial diversity of extant microbialites in Mexico and Cuba. *Frontiers in microbiology* **9**, 510 (2018).

17. Centeno, C. M. *et al.* Microbialite genetic diversity and composition relate to environmental variables. *FEMS microbiology ecology* **82**, 724–735 (2012).

18. Myshrall, K. L. *et al.* Biogeochemical cycling and microbial diversity in the thrombolitic microbialites of Highborne Cay, Bahamas. *Geobiology* **8**, 337–354 (2010).

19. Dupraz, C. & Visscher, P. T. Microbial lithification in marine stromatolites and hypersaline mats. *Trends in Microbiology* **13**, 429–438 (2005).

20. Sabbe, K., Verleyen, E., Hodgson, D. A., Vanhoutte, K. & Vyverman, W. Benthic diatom flora of freshwater and saline lakes in the Larsemann Hills and Rauer Islands, East Antarctica. *Antarctic science* **15**, 227–248 (2003).

21. Patterson, D. J. & Simpson, A. G. Heterotrophic flagellates from coastal marine and hypersaline sediments in Western Australia. *European Journal of Protistology* **32**, 423–448 (1996).

22. Hauer, G. & Rogerson, A. Heterotrophic Protozoa from Hypersaline Environments. in *Adaptation to Life at High Salt Concentrations in Archaea, Bacteria, and Eukarya* (eds. Gunde-Cimerman, N., Oren, A. & Plemenitaš, A.) vol. 9 519–539 (Springer-Verlag, Berlin/Heidelberg, 2005).

23. Post, F. J., Borowitzka, L. J., Borowitzka, M. A., Mackay, B. & Moulton, T. The protozoa of a Western Australian hypersaline lagoon. *Hydrobiologia* **105**, 95–113 (1983).

24. Toneatti, D. M., Albarracín, V. H., Flores, M. R., Polerecky, L. & Farías, M. E. Stratified bacterial diversity along physico-chemical gradients in high-altitude modern stromatolites. *Frontiers in Microbiology* **8**, 1–12 (2017).

25. Wong, H. L., Smith, D. L., Visscher, P. T. & Burns, B. P. Niche differentiation of bacterial communities at a millimeter scale in Shark Bay microbial mats. *Scientific Reports* **5**, 1–17 (2015).

26. Shoemaker, A. *et al.* Wood–Ljungdahl pathway encoding anaerobes facilitate low-cost primary production in hypersaline sediments at Great Salt Lake, Utah. *FEMS Microbiology Ecology* **100**, fiae105 (2024).

27. Wong, H. L., MacLeod, F. I., White, R. A., Visscher, P. T. & Burns, B. P. Microbial dark matter filling the niche in hypersaline microbial mats. *Microbiome* **8**, 135 (2020).

28. Saghaï, A. *et al.* Comparative metagenomics unveils functions and genome features of microbialite associated communities along a depth gradient. *Environmental Microbiology* **18**, 4990–5004 (2016).

29. Gutiérrez-Preciado, A. *et al.* Functional shifts in microbial mats recapitulate early Earth metabolic transitions. *Nat Ecol Evol* **2**, 1700–1708 (2018).

30. Ragsdale, S. W. & Pierce, E. Acetogenesis and the Wood–Ljungdahl pathway of CO2 fixation. *Biochimica et Biophysica Acta (BBA)-Proteins and Proteomics* **1784**, 1873–1898 (2008).

31. Fuchs, G. Alternative Pathways of Carbon Dioxide Fixation: Insights into the Early Evolution of Life? *Annu. Rev. Microbiol.* **65**, 631–658 (2011).

32. Campbell, M. A. *et al.* Functional gene expression in Shark Bay hypersaline microbial mats: adaptive responses. *Frontiers in Microbiology* **11**, 560336 (2020).

33. Bernstein, H. C. *et al.* Trade-offs between microbiome diversity and productivity in a stratified microbial mat. *The ISME journal* **11**, 405–414 (2017).

34. Moorhead, D. L., Wolf, C. F. & Wharton, R. A. Impact of light regimes on productivity patterns of benthic microbial mats in an antarctic lake: A modeling study. *Limnology & Oceanography* **42**, 1561–1569 (1997).

35. Williams, T. J., Allen, M. A., Berengut, J. F. & Cavicchioli, R. Shedding light on microbial “dark matter”: insights into novel Cloacimonadota and Omnitrophota from an Antarctic Lake. *Frontiers in Microbiology* **12**, 741077 (2021).

36. Li, Y., Liu, H., Xiao, Y. & Jing, H. Metagenome sequencing and 982 microbial genomes from Kermadec and Diamantina Trenches sediments. *Scientific Data* **11**, 1067 (2024).

37. Fang, Y. *et al.* Casting Light on the Adaptation Mechanisms and Evolutionary History of the Widespread Sumerlaeota. *mBio* **12**, e00350-21 (2021).

38. Edgcomb, V. P. *et al.* Active eukaryotes in microbialites from Highborne Cay, Bahamas, and Hamelin Pool (Shark Bay), Australia. *The ISME journal* **8**, 418–429 (2014).

39. Couradeau, E. *et al.* Prokaryotic and eukaryotic community structure in field and cultured microbialites from the alkaline Lake Alchichica (Mexico). *PloS one* **6**, e28767 (2011).

40. Bonacolta, A. M., Visscher, P. T., Del Campo, J. & White III, R. A. The eukaryome of modern microbialites reveals distinct colonization across aquatic ecosystems. *npj Biofilms and Microbiomes* **10**, 78 (2024).

41. Breitbart, M. *et al.* Metagenomic and stable isotopic analyses of modern freshwater microbialites in Cuatro Ciénegas, Mexico. *Environmental Microbiology* **11**, 16–34 (2009).

42. Kanik, M. *et al.* Unexpected Abundance and Diversity of Phototrophs in Mats from Morphologically Variable Microbialites in Great Salt Lake, Utah. *Appl Environ Microbiol* **86**, e00165-20 (2020).

43. Ricci, F. *et al.* Fine□scale mapping of physicochemical and microbial landscapes of the coral skeleton. *Environmental Microbiology* 1462-2920.16369 (2023) doi:10.1111/1462-2920.16369.

44. Larsen, M., Borisov, S. M., Gunwald, B., Klimant, I. & Glud, R. N. A simple and inexpensive, high-resolution color-ratiometric planar optode imaging approach: Application to oxygen and pH sensing. *Limnology and Oceanography: Methods* **2**, 348–360 (2011).

45. Hall, N. *et al.* Aerotolerant methanogens use seaweed and seagrass metabolites to drive marine methane emissions. *bioRxiv* 2024–10 (2024).

46. Martínez-Alonso, M. *et al.* Distribution of phototrophic populations and primary production in a microbial mat from the Ebro Delta, Spain. *International Microbiology* **7**, 19–25 (2004).

47. Canfield, D. E. & Des Marais, D. J. Biogeochemical cycles of carbon, sulfur, and free oxygen in a microbial mat. *Geochimica et Cosmochimica acta* **57**, 3971–3984 (1993).

48. Kurth, D. *et al.* Arsenic metabolism in high altitude modern stromatolites revealed by metagenomic analysis. *Scientific reports* **7**, 1024 (2017).

49. Prywes, N., Phillips, N. R., Tuck, O. T., Valentin-Alvarado, L. E. & Savage, D. F. Rubisco Function, Evolution, and Engineering. *Annu. Rev. Biochem.* **92**, 385–410 (2023).

50. Garritano, A. N., Song, W. & Thomas, T. Carbon fixation pathways across the bacterial and archaeal tree of life. *PNAS nexus* **1**, pgac226 (2022).

51. Fuchs, G. CO2 fixation in acetogenic bacteria: variations on a theme. *FEMS Microbiology Reviews* **2**, 181–213 (1986).

52. Loreau, M. & Hector, A. Partitioning selection and complementarity in biodiversity

experiments. *Nature* **412**, 72–76 (2001).

53. Cardinale, B. J. *et al.* Effects of biodiversity on the functioning of trophic groups and ecosystems. *Nature* **443**, 989–992 (2006).

54. Dunham, E. C. *et al.* An ecological perspective on dolomite formation in Great Salt Lake, Utah. *Frontiers in Earth Science* **8**, 24 (2020).

55. Seto, M. & Iwasa, Y. Microbial material cycling, energetic constraints and ecosystem expansion in subsurface ecosystems. *Proc. R. Soc. B.* **287**, 20200610 (2020).

56. Last, W. M. & De Deckker, P. Modern and Holocene carbonate sedimentology of two saline volcanic maar lakes, southern Australia. *Sedimentology* **37**, 967–981 (1990).

57. Bolyen, E. *et al.* Reproducible, interactive, scalable and extensible microbiome data science using QIIME 2. *Nature biotechnology* **37**, 852–857 (2019).

58. Martin, M. Cutadapt removes adapter sequences from high-throughput sequencing reads. *EMBnet. journal* **17**, 10–12 (2011).

59. Callahan, B. J. *et al.* DADA2: High-resolution sample inference from Illumina amplicon data. *Nature Methods* **13**, 581–583 (2016).

60. Quast, C. *et al.* The SILVA ribosomal RNA gene database project: improved data processing and web-based tools. *Nucleic acids research* **41**, D590–D596 (2012).

61. Salazar, V. W. *et al.* Metaphor—a workflow for streamlined assembly and binning of metagenomes. *GigaScience* **12**, giad055 (2023).

62. Chen, S. Ultrafast one□pass FASTQ data preprocessing, quality control, and deduplication using fastp. *Imeta* **2**, e107 (2023).

63. Li, D., Liu, C.-M., Luo, R., Sadakane, K. & Lam, T.-W. MEGAHIT: an ultra-fast single-node solution for large and complex metagenomics assembly via succinct de Bruijn graph. *Bioinformatics* **31**, 1674–1676 (2015).

64. Nissen, J. N. *et al.* Improved metagenome binning and assembly using deep variational autoencoders. *Nat Biotechnol* **39**, 555–560 (2021).

65. Kang, D. D. *et al.* MetaBAT 2: an adaptive binning algorithm for robust and efficient genome reconstruction from metagenome assemblies. *PeerJ* **7**, e7359 (2019).

66. Alneberg, J. *et al.* Binning metagenomic contigs by coverage and composition. *Nature methods* **11**, 1144–1146 (2014).

67. Sieber, C. M. K. *et al.* Recovery of genomes from metagenomes via a dereplication, aggregation and scoring strategy. *Nature Microbiology* **3**, 836–843 (2018).

68. Olm, M. R., Brown, C. T., Brooks, B. & Banfield, J. F. dRep: a tool for fast and accurate genomic comparisons that enables improved genome recovery from metagenomes through de-replication. *The ISME Journal* **11**, 2864–2868 (2017).

69. Chklovski, A., Parks, D. H., Woodcroft, B. J. & Tyson, G. W. CheckM2: a rapid, scalable and accurate tool for assessing microbial genome quality using machine learning. *Nature Methods* **20**, 1203–1212 (2023).

70. Bowers, R. M. *et al.* Minimum information about a single amplified genome (MISAG) and a metagenome-assembled genome (MIMAG) of bacteria and archaea. *Nature biotechnology* **35**, 725–731 (2017).

71. Parks, D. H. *et al.* GTDB: an ongoing census of bacterial and archaeal diversity through a phylogenetically consistent, rank normalized and complete genome-based taxonomy. *Nucleic acids research* **50**, D785–D794 (2022).

72. Chaumeil, P.-A., Mussig, A. J., Hugenholtz, P. & Parks, D. H. GTDB-Tk v2: memory friendly classification with the genome taxonomy database. *Bioinformatics* **38**, 5315–5316 (2022).

73. Hyatt, D. *et al.* Prodigal: prokaryotic gene recognition and translation initiation site identification. *BMC Bioinformatics* **11**, 119 (2010).

74. Altschul, S. F. *et al.* Gapped BLAST and PSI-BLAST: a new generation of protein database search programs. *Nucleic Acids Research* **25**, 3389–3402 (1997).

75. Greening, C. Greening lab metabolic marker gene databases. (2021).

76. Shaffer, M. *et al.* DRAM for distilling microbial metabolism to automate the curation of microbiome function. *Nucleic acids research* **48**, 8883–8900 (2020).

77. Buchfink, B., Xie, C. & Huson, D. H. Fast and sensitive protein alignment using DIAMOND. *Nature methods* **12**, 59–60 (2015).

78. Kalyaanamoorthy, S., Minh, B. Q., Wong, T. K., Von Haeseler, A. & Jermiin, L. S. ModelFinder: fast model selection for accurate phylogenetic estimates. *Nature methods* **14**, 587–589 (2017).

79. Minh, B. Q. *et al.* IQ-TREE 2: new models and efficient methods for phylogenetic inference in the genomic era. *Molecular biology and evolution* **37**, 1530–1534 (2020).

80. Hoang, D. T., Chernomor, O., Von Haeseler, A., Minh, B. Q. & Vinh, L. S. UFBoot2: improving the ultrafast bootstrap approximation. *Molecular biology and evolution* **35**, 518–522 (2018).

81. Edgar, R. C. Muscle5: High-accuracy alignment ensembles enable unbiased assessments of sequence homology and phylogeny. *Nature Communications* **13**, 6968 (2022).

82. Letunic, I. & Bork, P. Interactive Tree of Life (iTOL) v6: recent updates to the phylogenetic tree display and annotation tool. *Nucleic Acids Research* gkae268 (2024).

83. Islam, Z. F. *et al.* Two Chloroflexi classes independently evolved the ability to persist on atmospheric hydrogen and carbon monoxide. *ISME J* **13**, 1801–1813 (2019).

84. Rice, E. W., Bridgewater, L. & Association, A. P. H. *Standard Methods for the Examination of Water and Wastewater*. vol. 10 (American public health association Washington, DC, 2012).

85. Davis, N. M., Proctor, D. M., Holmes, S. P., Relman, D. A. & Callahan, B. J. Simple statistical identification and removal of contaminant sequences in marker-gene and metagenomics data. *Microbiome* **6**, 1–14 (2018).

86. Wickham, H. ggplot2. *WIREs Computational Stats* **3**, 180–185 (2011).

87. McMurdie, P. J. & Holmes, S. phyloseq: an R package for reproducible interactive analysis and graphics of microbiome census data. *PloS one* **8**, e61217 (2013).

88. Dixon, P. VEGAN, a package of R functions for community ecology. *Journal of vegetation science* **14**, 927–930 (2003).

Figures legend

Figure 1 | Maximum-likelihood genome trees depicting the taxonomic diversity of 331 archaeal and bacterial metagenome-assembled genomes (MAGs), built with 1000 ultrafast bootstrap replicates using the LG+C10+F+G and WAG+G20 models, respectively. The top heatmap highlights the metabolic potential of microbes co-encoding energy acquisition enzymes with carbon fixation pathways. The side bargraph shows the number of MAGs in each microbial family (GTDB taxonomy). The bottom heatmap shows the abundance of each gene in the metagenomic short reads in West Basin Lake samples (bold) and across 17 publicly available microbialite community metagenomes from five global sites. Homology-based searches were used to identify signature genes encoding enzymes associated with metabolic pathways. To infer abundance, read counts were normalised to gene length and the abundance of single-copy marker genes.

Figure 2 | Metabolic model predicted based on genome- and gene-resolved data of the dominant microbial guilds within the microbialite communities of West Basin Lake. This model represents the inferred metabolic pathways and interactions based on the genomic content of these guilds. Blue and brown lines indicate the direction of electron acceptors and donors, respectively. Note that the graphic is an artistic generalization of the data and should not be interpreted as an exact depiction of the microbial community structure. Asterisk (*) denotes that specific metabolic marker genes were exclusively recovered from metagenomic short-read data.

Figure 3 | Biogeochemical assays illustrating the metabolic activities of microbialite communities under aerobic (**a**) and anaerobic (**b**, **c**) conditions in microcosms. Oxygen dynamics were assessed using chemical imaging on independent microbialite samples incubated in 4 L glass aquaria, with data presented as the mean ± standard deviation for defined photosynthetic regions of interest. Trace gases, sulfide and ferrous ion measurements were taken in 120 ml sealed serum vial containing 10 g of microbialite slurry and 50 mL of 0.22 µm-filtered lake water. Trace gas microcosms were supplemented with 10 ppm H_2, CH_4, and CO in the headspace. S^{2-} and Fe^{2+} microcosms were supplied with either 100 µM $Na_2S{\cdot}9H_2O$ (only for consumption) or 6 mM $FeCl_2$. All anaerobic microcosms except for S^{2-} production were supplemented with 1.5 mM NO_3^- as an electron acceptor. Nitrification (NOx = NO_2^- + NO_3^-) measurements were taken in uncapped 250 mL Schott bottles containing approximately 10 g of microbialite slurry, 100 mL of 0.22 µm-filtered lake water and 100 µM NH_4^+. In the oxygen plot, asterisks (*) indicate the time when light was switched off, mimicking the onset of darkness. All microcosm experiments were performed in triplicate, with results expressed as the mean ±

standard deviation across three replicates. All measurements except for oxygen dynamics were normalised to microbialite slurry wet weight.

Figure 4 | Maximum-likelihood phylogenetic trees of 140 RbcL (**a**), 184 AcsB (**b**), and 36 AclB (**c**) amino acid sequences obtained from the three microbialite samples, constructed using 1000 ultrafast bootstrap replicates. The LG+R5 (**a**), LG+F+I+R6 (**b**), and LG+I+G4 (**c**) substitution models were applied. Sequences derived from binned contigs are highlighted in bold, while those from unbinned contigs are shown without emphasis. Bootstrap support values ≥ 90 are denoted by white circles (**a–c**). Panel (**d**) Credible intervals of effect (electron donors) relative to dark condition denoting 2.5th and 97.5th (thin bar) and 25th and 75th (thick bar) percentiles of posterior probability of the effect of each assay condition relative to the dark condition.

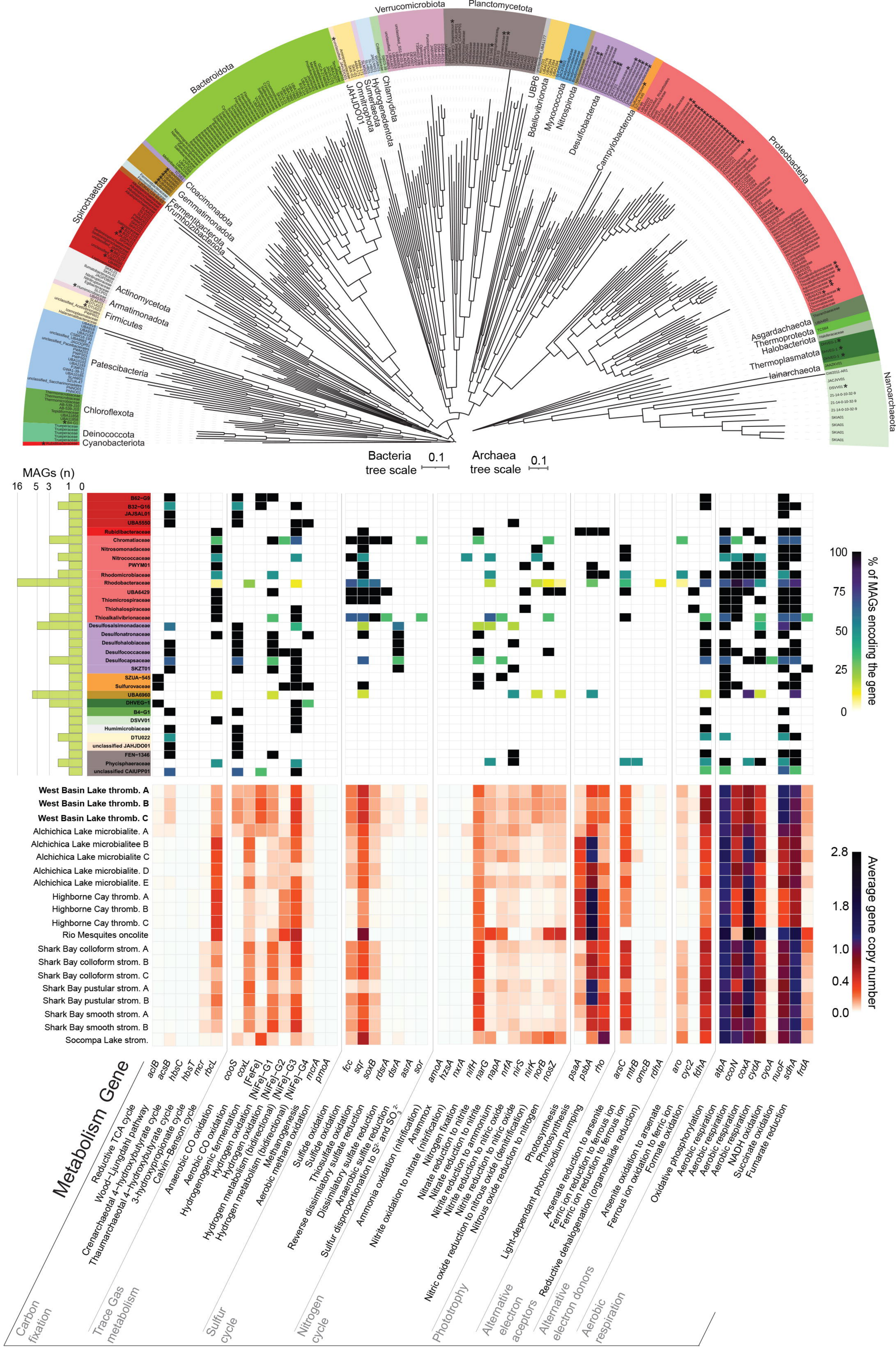
Bacteroidota
Verrucomicrobiota
Planctomycetota
Chlamydiota
Hydrogenedentota
Sumerlaeota
Omnitrophota
JAHJDO01
UBP6
Bdellovibrionota
Myxococcota
Nitrospinota
Desulfobacterota
Campylobacterota
Proteobacteria
Spirochaetota
Cloacimonadota
Gemmatimonadota
Fermentibacterota
Krumholzibacteriota
Actinomycetota
Armatimonadota
Firmicutes
Patescibacteria
Chloroflexota
Deinococcota
Cyanobacteriota
Asgardachaeota
Thermoproteota
Halobacteriota
Thermoplasmatota
Iainarchaeota
Nanoarchaeota
Bacteria tree scale 0.1
Archaea tree scale 0.1
MAGs (n)
16 5 3 1 0
B62-G9
B32-G16
JAJSAL01
UBA5550
Rubidibacteraceae
Chromatiaceae
Nitrosomonadaceae
Nitrococcaceae
PWYM01
Rhodomicrobiaceae
Rhodobacteraceae
UBA6429
Thiomicrospiraceae
Thiohalospiraceae
Thioalkalivibrionaceae
Desulfosalsimonadaceae
Desulfonatronaceae
Desulfohalobiaceae
Desulfococcaceae
Desulfocapsaceae
SKZT01
SZUA-545
Sulfurovaceae
UBA6960
DHVEG-1
B4-G1
DSVV01
Humimicrobiaceae
DTU022
unclassified JAHJDO01
FEN-1346
Phycisphaeraceae
unclassified CAIUPP01
West Basin Lake thromb. A
West Basin Lake thromb. B
West Basin Lake thromb. C
Alchichica Lake microbialite. A
Alchichica Lake microbialitee B
Alchichica Lake microbialite C
Alchichica Lake microbialite. D
Alchichica Lake microbialite. E
Highborne Cay thromb. A
Highborne Cay thromb. B
Highborne Cay thromb. C
Rio Mesquites oncolite
Shark Bay colloform strom. A
Shark Bay colloform strom. B
Shark Bay colloform strom. C
Shark Bay pustular strom. A
Shark Bay pustular strom. B
Shark Bay smooth strom. A
Shark Bay smooth strom. B
Socompa Lake strom.
100
75
50
25
0
% of MAGs encoding the gene
2.8
1.8
1.0
0.4
0.0
Average gene copy number
Metabolism Gene
aclB acsB hbsC hbsT mcr rbcL
cooS coxL [FeFe] [NiFe]-G1 [NiFe]-G2 [NiFe]-G3 [NiFe]-G4 mcrA pmoA
fcc sqr soxB rdsrA dsrA asrA sor
amoA hzsA nxrA nifH narG napA nrfA nirS nirK norB nosZ
psaA psbA rho
arsC mtrB omcB rdhA
aro cyc2 fdhA
atpA ccoN coxA cydA cyoA nuoF sdhA frdA
Reductive TCA cycle
Wood-Ljungdahl pathway
Crenarchaeotal 4-hydroxybutyrate cycle
Thaumarchaeotal 4-hydroxybutyrate cycle
3-hydroxypropionate cycle
Calvin-Benson cycle
Anaerobic CO oxidation
Aerobic CO oxidation
Hydrogenogenic fermentation
Hydrogen oxidation
Hydrogen oxidation (bidirectional)
Hydrogen metabolism (bidirectional)
Methanogenesis
Aerobic methane oxidation
Sulfide oxidation
Sulfide oxidation
Thiosulfate oxidation
Reverse dissimilatory sulfate reduction
Dissimilatory sulfate reduction
Anaerobic sulfite reduction
Sulfur disproportionation to S2- and SO3 2-
Ammonia oxidation (nitrification)
Anammox
Nitrite oxidation to nitrate (nitrification)
Nitrogen fixation
Nitrate reduction to nitrite
Nitrate reduction to nitrite
Nitrite reduction to ammonium
Nitrite reduction to nitric oxide
Nitrite reduction to nitric oxide
Nitrite reduction to nitric oxide (denitrification)
Nitrous oxide reduction to nitrogen
Nitric oxide reduction to nitrous oxide
Photosynthesis
Photosynthesis
Light-dependant photon/sodium pumping
Arsenate reduction to arsenite
Ferric ion reduction to ferrous ion
Ferric ion reduction to ferrous ion
Reductive dehalogenation (organohalide reduction)
Arsenite oxidation to arsenate
Ferrous ion oxidation to ferric ion
Formate oxidation
Oxidative phosphorylation
Aerobic respiration
Aerobic respiration
Aerobic respiration
Aerobic respiration
NADH oxidation
Succinate oxidation
Fumarate reduction
Carbon fixation
Trace Gas metabolism
Sulfur cycle
Nitrogen cycle
Phototrophy
Alternative electron aceptors
Alternative electron donors
Aerobic respiration

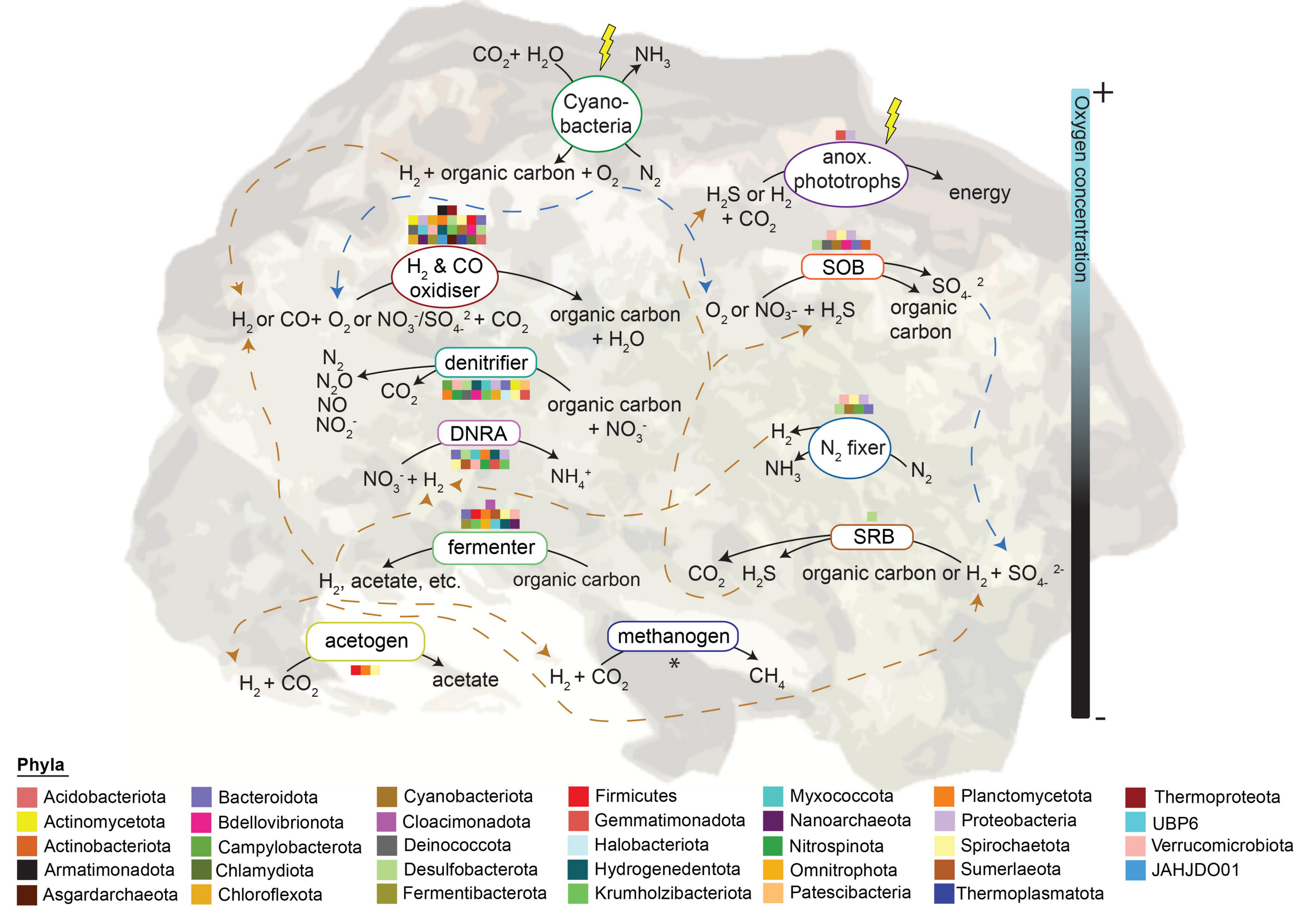
CO2 + H2O
NH3
Cyano-bacteria
H2 + organic carbon + O2
N2
anox. phototrophs
H2S or H2 + CO2
energy
H2 & CO oxidiser
H2 or CO + O2 or NO3-/SO4 2- + CO2
organic carbon + H2O
SOB
O2 or NO3- + H2S
SO4 2-
organic carbon
denitrifier
N2
N2O
NO
NO2-
CO2
organic carbon + NO3-
DNRA
NO3- + H2
NH4+
H2
NH3
N2 fixer
N2
fermenter
H2, acetate, etc.
organic carbon
SRB
CO2
H2S
organic carbon or H2 + SO4 2-
acetogen
H2 + CO2
acetate
methanogen
H2 + CO2
*
CH4
Oxygen concentration
+
-
Phyla
Acidobacteriota
Actinomycetota
Actinobacteriota
Armatimonadota
Asgardarchaeota
Bacteroidota
Bdellovibrionota
Campylobacterota
Chlamydiota
Chloroflexota
Cyanobacteriota
Cloacimonadota
Deinococcota
Desulfobacterota
Fermentibacterota
Firmicutes
Gemmatimonadota
Halobacteriota
Hydrogenedentota
Krumholzibacteriota
Myxococcota
Nanoarchaeota
Nitrospinota
Omnitrophota
Patescibacteria
Planctomycetota
Proteobacteria
Spirochaetota
Sumerlaeota
Thermoplasmatota
Thermoproteota
UBP6
Verrucomicrobiota
JAHJDO01

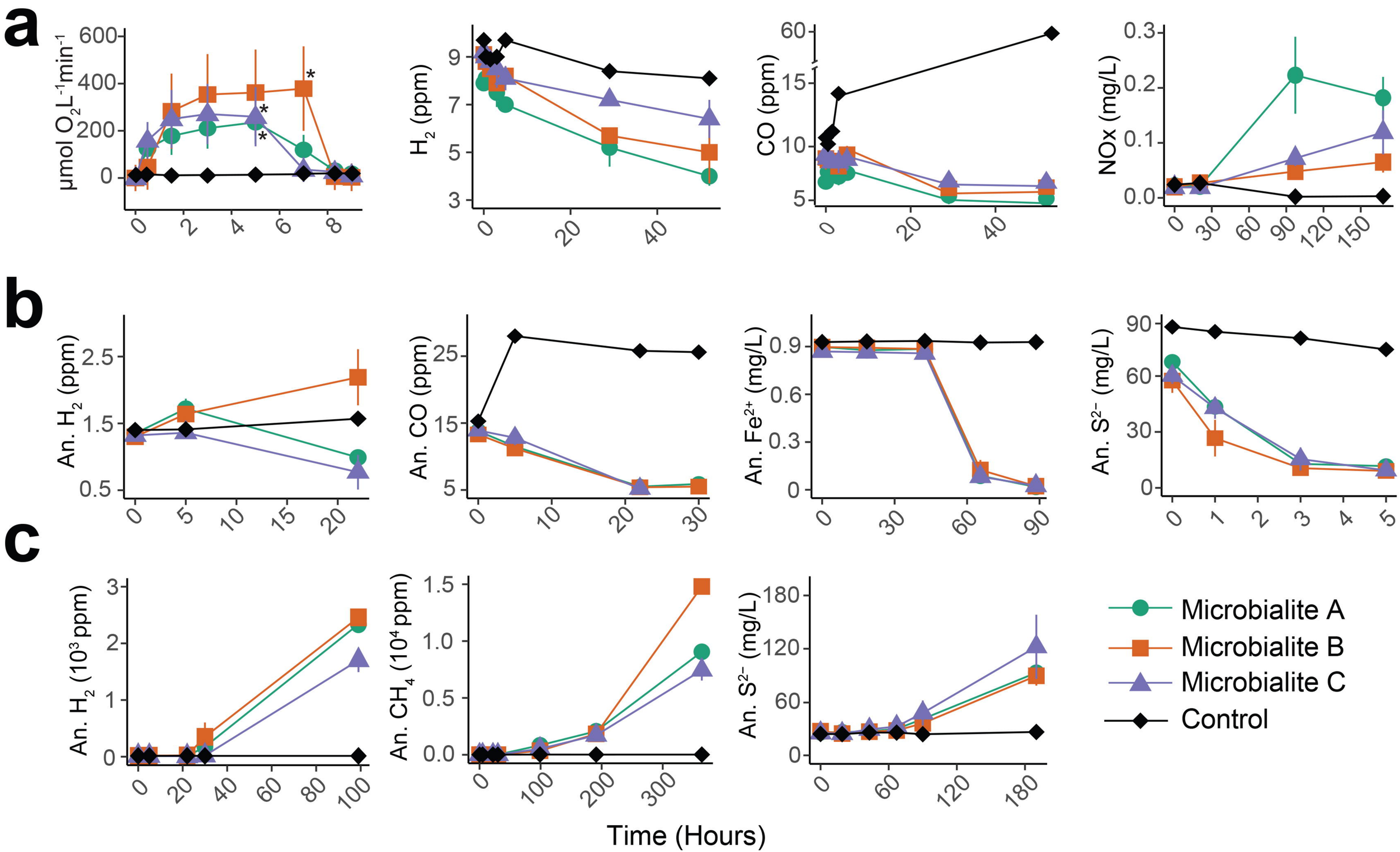
a
b
c
μmol O2L-1min-1
H2 (ppm)
CO (ppm)
NOx (mg/L)
An. H2 (ppm)
An. CO (ppm)
An. Fe2+ (mg/L)
An. S2- (mg/L)
An. H2 (10³ ppm)
An. CH4 (10⁴ ppm)
An. S2- (mg/L)
Time (Hours)
Microbialite A
Microbialite B
Microbialite C
Control

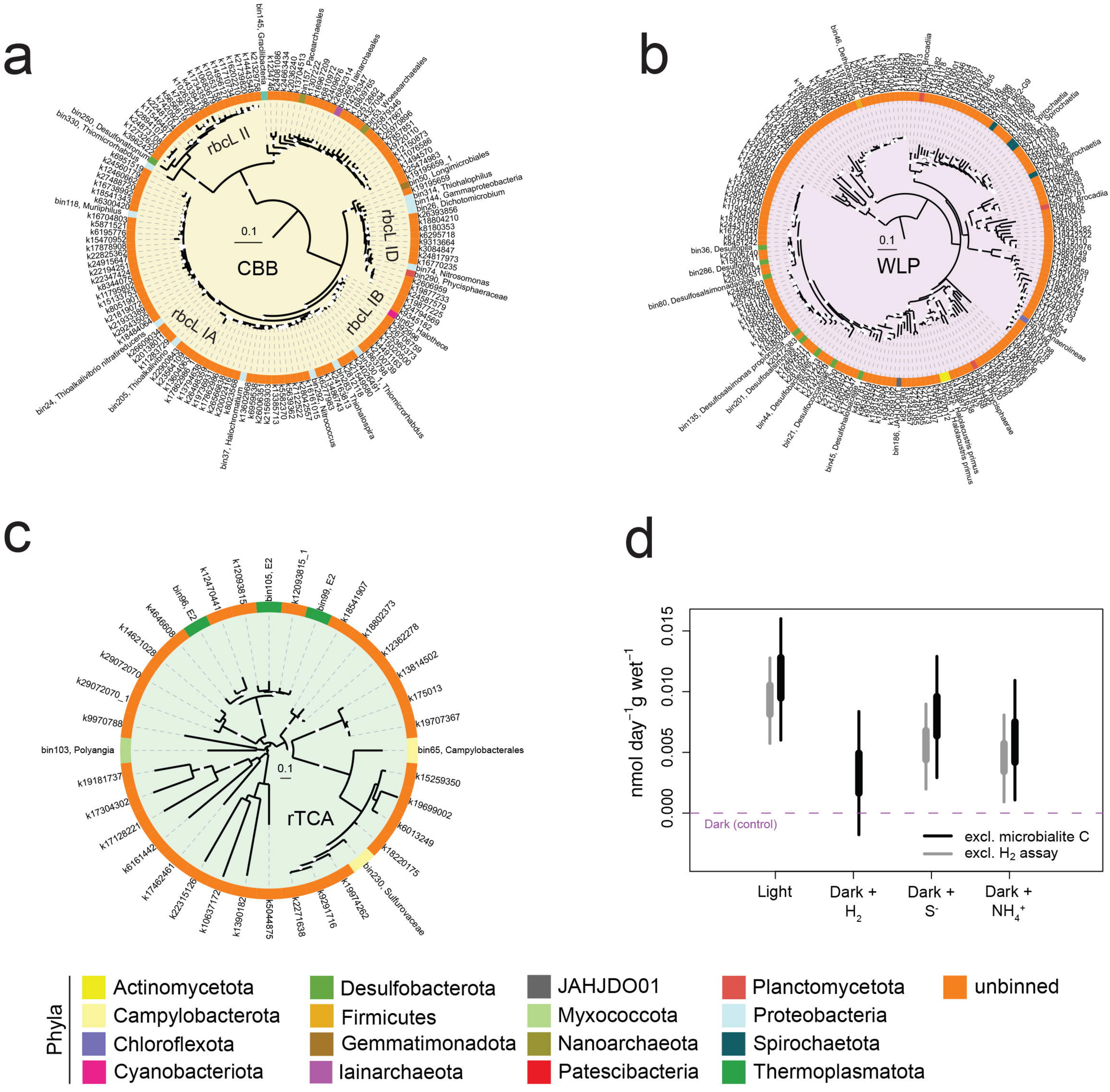
a
CBB
0.1
rbcL II
rbcL ID
rbcL IB
rbcL IA
bin145, Gracilibacteria
bin157, Pacearchaeales
bin266, Iainarchaeales
bin53, Woesearchaeales
bin250, Desulfonatronum
bin330, Thiomicrorhabdus
bin118, Muriiphilus
bin50, Longimicrobiales
bin314, Thiohalophilus
bin144, Gammaproteobacteria
bin26, Dichotomicrobium
bin74, Nitrosomonas
bin290, Phycisphaeraceae
bin62, Halothece
bin24, Thioalkalivibrio nitratireducens
bin205, Thioalkalivibrio
bin37, Halochromatium
bin292, Nitrococcus
bin283, Thiohalospira
bin330_1, Thiomicrorhabdus
b
WLP
0.1
bin46, Deltaproteobacteria
bin36, Desulfopila
bin286, Desulfopila
bin80, Desulfosalsimonadaceae
bin135, Desulfosalsimonas propionicica
bin201, Desulfosalsimonas
bin44, Desulfobacteraceae
bin21, Desulfococcaceae
bin45, Desulfohalobiaceae
bin186, JAHJDO01
bin55, Haloplasmatales
Haloplasmatales
Haloplasmatales